Chapter 3

Modulation on Current Distribution in the Pinched Base Region Corresponding to Collector Doping Profiles and the Correlated Impacts in DC and RF Characteristics

Preface

In this Chapter, the physical behavior and the associated impacts of base resistance r_B of the modern SiGe HBT devices upon the biasing current were discussed. Including the device geometry, doping profile and bias condition, which impacted the base resistance r_B were set as main variables in this study. Several efforts have been done in this research including the SiGe HBT devices fabrications, testing and simulation. The results showed that the r_B values could be increased with increasing collector current under the relative low current biasing levels and then fall down on higher ones. It was also found that such phenomenon could become event significant as the total emitter area shrinks Furthermore, it was also discovered that the collector doping levels could modulate the bias dependency of the base r resistance, too. After analyzing, two mechanisms could be involved in this phenomenon: the vertical current spreading and vertical current crowding effects. The deductions have been verified by the simulation and measurement results. Furthermore, it was also verified that the behavior of r_B could lead to the inconsistency of the collector current density levels on which peak f_T and peak f_{max} took place.

3.0 Introduction

Technologies for fabricating high device f_T, f_{max}, low frequency (1/f) as well as microwave noise, power efficiency and low intermodulation would be desired for wireless communication applications. Silicon germanium hetero-junction bipolar transistor (SiGe HBT), with its nature potential, would be capable of providing such performances. However, the base resistance of the HBT devices could suffer the above-mentioned parameters. Numbers of studies have been done dedicating on the technique to extract the values of r_B [1-5]. Unfortunately, analysis on the physical origins corresponding to the base resistance and the associated impacts on device RF characteristics were necessary for even critical applications, especially for low power, and high efficiency RF circuits. In this chapter, the bias dependency of r_B and the associated influences on the RF characteristics was discussed, as well as the improving strategies. In section 3.1, the current dependent characteristics of the base resistance r_B was illustrated. Next, in section 3.2, the techniques and associated information involved corresponding to the vertical current spreading and crowding effect would be described including the measurement results and the deduction and identification of the associating physical model. Third, in section 3.3, the theoretic deduction on the base dependent behavior of r_B discussed in 3.2 was presented. The associated deductions were also identified by device simulation in section 3.3. In section 3.4, the impacts resulting from the current dependent r_B behavior on the RF characteristics of the modern HBT devices in various geometry and collector doping profile based on the measurement results were reported. Moreover, for accurately verification in numerical way, the mathematical relations of f_T and f_{max} based on the proper device RF model should be required. In section 3.5, the derivation details of the mathematical relations based on the RF HBT model with the emitter resistance was illustrated. Furthermore, the RF characteristic impacts from the bias dependent behaviors of r_B described in section 3.4 were verified by the numerical approaches associated with the measurement results which were applied to verify the scheme of the impacts. Finally, in section 3.6, the impact of the current dependency of r_B on the device noise characteristics would be discussed.

3.1 Current Dependency of the Base Resistance

(a) Technology

SiGe HBT with multi-emitter strip configurations was fabricated by 130 GHz technology. Poly-emitter structure, one of the approaches to enhance the performance of SiGe HBT device in this study was used to increase the emitter doping concentration, so as to increase the device current gain. Self-align technology, another approach adopted in this study was applied to reduce the external overlapping capacitance and base resistance while the poly-emitter device structure was being applied. Such technique enhances the high frequency performance and yielding higher cutoff frequency of the device. Furthermore, to improve the high current injection characteristics associated with Kirk effect, the selective implant collector (SIC) layer was performed by higher concentration above the n-type epitaxy layer between the collector and buried layer. As for the lossy nature of silicon substrate, especially for RF signal, isolation structure with high cross-talk rejection must be available for technological focus on RF applications. Deep trench isolation technique , one of the isolation technologies was applied in our technology to provide significant isolation performance.

(b) Testing Samples

SiGe HBT devices with different geometries were fabricated in this study and listed in Table 3.1 with the corresponding name list. Figure 3.1 (a), (b) and (c) illustrated the schematics of cross-section, top view and doping profile of the HBT devices. There were three groups of devices denoted as group H, M and L involved in this research and devices in the same group are in fixed doping profiles. The doping profiles of H, M and L devices were different in the collector region so as to their operation speeds. Regarding to H and M groups there were selective implant collector (SIC) structures within the base and buried layer for improving the Kirk effect while such structure was not available for L group. In addition, the doping concentration of SIC layer for M group was lighter compared to that of H group and it resulted in lower cutoff frequency than H group. In each group, devices' geometries were different in emitter strip number, emitter widths or lengths. The names of the testing samples were given in, H_xyz, M_xyz and L_xyz. X denotes the strip numbers of HBT devices. Parameters y and z are mapped into the corresponding samples through Table 3.1. For example, the medium-speed device M212 has 2 emitter strips. Each strip of M212 has 0.2 μm in its emitter width and 1.76 μm in its emitter length. H435 denotes the high-speed HBT device with 4 emitter strips and each emitter is 0.4 μm in width and 10.16 μm in length.

(c) Measurement

The above mentioned devices were tested under various bias current levels to examine the RF properties. In order to maintain experimental objectivity and lowest forward transit time the swept value of V_{BE} and fixed V_{BC} of 1 volt (reverse bias) were applied to each testing HBT device. The collector resistance r_C and emitter resistance r_E and were tested by the standard fly-back measurement methodologies [7]. As to the base-colletor capacitance C_{BC} and the input resistance r_{BE} of the devices were tested and extracted by standard DC and RF parameter procedure [7]. The concepts for extracting the base-to-emitter resistance r_{BE} were also well known and illustrated in [7].

(d) Bias Dependent Behavior of the Base Resistance

Figures 3.3 (a), (b) and (c) illustrated the relationships between the base resistances r_B of HBT devices and the corresponding biasing current density levels. The values of the emitter resistance (r_E) were listed in Table 3.2. In Fig. 3.3 (a), the base resistance r_B of devices with fixed emitter length (L_E) for 10.16 μm and various emitter widths (W_E) for 0.2, 0.3, 0.4 and 0.9 μm were presented with the various emitter strip numbers (N_E). It was observed that for M_115, M125 and M_135, the resistance values were increased with increasing current density and each of them had a peak on the specific higher current levels. Such phenomena on lower current levels behaved less significantly as the emitter widths increased. As the emitter width increased to 0.9 μm (M_145), the above phenomena would even disappear. Besides, from Fig. 3.3 (a), the devices with more emitter strips would also result in less resistance growing as the collector current density increased. In Figure 3.3 (b), r_B of devices with fixed W_E (0.2 μm) and various L_E (0.76, 1.76, 2.64, 4.52 and 10.16 μm) was presented with fixed emitter strip number of the unity. The phenomenon that r_B raised on lower current levels would become less apparent as the emitter length increased. In Fig. 3.3 (c), the r_B-I_C relationships of devices in groups H, M and L were illustrated and there were three devices for each group. As for the devices in the same geometry, the values of their r_B were approximately the similar but split from each other as the biasing current increased. It was observed that the devices in group L showed less significant r_B rising effect than the other two groups in the same geometries, while the H group devices behaved of the most consequence. In addition, the behavior divergence in devices of H, M and L group would be further apparent as the emitter length L_E shrank.

Based on the phenomena observed from Figs. 3.3 (a), (b) and (c), some preliminary summaries were concluded. First, as the emitter width decreased, although the value of r_B would be decreased, the r_B rising phenomenon became even significant. Next, as the emitter length increased, such phenomenon was weakened. Moreover, such phenomenon could be enhanced for the devices with heavier collector doping concentration. In the following paragraph, the physical model would be created according to the summary mentioned above.

3.2 Associated Physics: Current Spreading and Crowding

Based on the phenomenon discussed above, the preliminary physical model to explain the bias current dependency of r_B was assumed. Figures 3.4 (a) and (b) help us to illustrate the associated physical concepts.

In Fig. 3.4 (a), the half cross-sections of view of the base-emitter structure of a group M device under relative low current density (J_{B1}), moderate high current density (J_{B2}) and high current levels (J_{B3}) bias conditions were presented respectively. The lines with the arrowheads in Fig. 3.4 (a) illustrated the current flux from the emitter-base junction through the intrinsic pinch base region to the poly-silicon base structure. The coordinates x = 0 and 0.15 μm denoted the horizontal location of the emitter center and base contact edge, respectively. On the other hand, the coordinates y = 0 denoted the vertical location on the interfaces between the poly-Si emitter and emitter drive-in region. The poly-Si emitter structure was about 3 μm thick with extremely high doping concentration. The dash lines, thin solid lines and thicker solid lines in Fig. 3.4 (a) illustrated the relative intensity of each current flux (solid lines > dash lines, thick lines > thin lines). In addition, in which the denser the flux lines were located, the larger current densities would be distributed there. In Fig. 3.4 (a), there were five main fluxes left from the five diodes on the E-B junction with the corresponding junction voltages V_{BE1}, V_{BE2}, V_{BE3}, V_{BE4} and V_{BE5}. They traveled along the associated current paths (P_1, P_2, P_3, P_4 and P_5) with the respective series resistance (R_1, R_2, R_3, R_4 and R_5) to the poly-Si base. Among these five current paths, the deeper the current path distributed, the larger series resistance resulting from the length of each paths for the carriers traveling from the emitter to the base region it provided ($R_1 < R_2 < R_3 < R_4 < R_5$). Furthermore, the sheet resistance was also larger toward in the deeper bulk region resulting from the concentration distribution of boron atoms (N_B) in the y direction as illustrated in Fig. 3.1 (c).

As the base current density (J_B) increased, the depth that the flux extended in the base region would be more profound. Such physics was deduced as the major mechanisms which dominated the current dependency of r_B on lower J_B levels (under J_{B3}) and such effect was denoted as vertical current spreading effect. It caused the increase of the value of r_B with increasing J_B as $J_B < J_{B3}$. On the contrary, the distribution current density in vertical direction would be less uniform and even more accumulated at $y = 0$ as J_B was increased. It resulted from the enlarged differences among V_{BE1}, V_{BE2}, V_{BE3}, V_{BE4} and V_{BE5} ($V_{BE1} < V_{BE2} < V_{BE3} < V_{BE4} < V_{BE5}$). As a result, the increasing ratio of current density on P_1, P_2, P_3, P_4 and P_5 would be more divergent (maximum on P_1 and minimum on P_5) as J_B was increased, especially on higher J_B levels. Similarly, it could be deduced as the major mechanism dominating the current dependency of r_B on higher J_B levels (above J_{B3}) and denoted as vertical current crowding effect. It resulted in decreasing the value of r_B with increasing J_B as $J_B > J_{B3}$. In other words, J_{B3} was denoted as the current level on which the above two mechanisms changed over.

Similar behaviors were deduced in devices of groups H and L. Correspondingly, the parameters J_{B1}', J_{B2}', J_{B3}' and J_{B1}", J_{B2}", J_{B3}" were denoted as the corresponding parameters in groups H and L compared to those of groups M. Since the doping concentration of SIC layer for H-devices was heavier compared with M-group, it resulted in the thinner intrinsic base. It forced the carriers in H-devices to flow in the lower resistive base region near the emitter as illustrated in Fig. 3.4 (b) and featured lower ramping-up slope of r_B values as J_B increased compared with M-devices. For this reason, the current level J_{B3}' in H-group devices would be larger than J_{B3} of M-group devices on which both aforementioned mechanisms would change over. On the contrary, there were no SIC layer in the device doping profile in L-group devices. The current fluxes would be forced to spread more profoundly than those of devices in groups H and M. It led to smaller value of J_{B3}" while being compared with the other groups.

In order to further confirm the model assumed in the above descriptions, we preliminarily examined it with the measured r_B of devices in various geometries. First, based on the model assumed, for the devices with the larger W_E, their vertical current spreading effect would become less apparent resulting from the larger lateral series resistance. It was because the vertical current spreading effect in Fig. 3.3 (a) would be taken place by vertical current crowding effect on the comparable lower J_{B_P} than the smaller W_E devices did. The physical meaning of J_{B_P} was compared to J_{B3} in the above discussion on which the peak value of r_B took place. Next, for the devices with the fixed W_E, they should have the same values of J_{B_P}, but the values of r_{B_P} would be decreased with increasing L_E or N_E. These aforementioned phenomena resulted simply from the paralleling effects of the emitters and such deduction from the model was consistent with the facts observed in Fig. 3.3 (b). Finally, in Fig. 3.3 (c), the behaviors upon the current dependency of r_B for the devices in groups H, M and L were consistent with the predictions based on the model assumed.

3.3 Physics Deductions, Simulations and Identifications

In the above paragraph, the consistence between the assumed current distribution model and r_B measurement results were identified. In this paragraph, the simulation results for further verifying the current distribution model would be presented. The MEDICI simulator, which has been widely popular in the electrical simulation for semiconductor devices, was applied in this model verification based on the calibrated secondary ion mass spectroscopy (SIMS) profile. The biasing conditions in simulations were set to be consistent with the ones applied in previous r_B measurements. Figures 3.4 (c) and (d) illustrated the current distribution profiles of devices M_113 and L_113 in coordinates x, y consisted with those in Figs. 3.4 (a) and (b), respectively. The current flux distribution profiles could directly reflect the behaviors of emitter and base resistance respectively.

In Fig. 3.4 (c), the current distribution along the lateral direction $J_1(x)$ and $J_2(x)$ on different y locations were illustrated. The solid lines illustrated $J_1(x)$ near the emitter-base edge y = 0.025 μm. In Fig. 3.4 (c), the current density was the highest at x = 0.1 μm and lowest at the emitter center x = 0 resulted in the well-known lateral current crowding effect [8, 9]. On the other hand, the dash lines in Fig. 3.4 (c) illustrated $J_2(x)$ on the middle vertical position in the poly-emitter structure (about 0.2 μm above the emitter-base junction) with extremely high arsenic doping concentration (above 10^{21} atoms/cm^3). Such high doping concentration made the poly-emitter structure behave conductor-liked electrically and resulted in relatively uniform current density distribution in the lateral direction on that vertical location. In addition, the ratios of the current density values between the various bias current levels were nearly fixed on each lateral location x. It caused that the value of the emitter resistance r_E would be nearly invariant to the bias current levels.

Figure 3.4 (d), by the way, illustrated the current distribution profiles $J_M(y)$ and $J_L(y)$ along the vertical direction of devices M_113 and L_113, respectively under various bias current levels J_C. On the bias current level of 10^{-5} A/cm^2, the shapes of both $J_M(y)$ and $J_L(y)$ were similar and relatively flat. As the current levels were increased to 10^{-3} A/cm^2, $J_L(y)$ expanded even deeper than $J_M(y)$. It was answered why the value of r_B began to rapidly increase for L_113 device while the r_B values of M_113 keep smoothly and slightly increasing as observed in Fig. 3.3 (c), and the value of r_B kept a relative low increasing slop for device M_113. As the current levels were continuously increased to 3×10^{-3} A/μm^2, the shape of $J_L(y)$ became much accumulated at y = 0.025 μm compared with $J_M(y)$. It seemed reasonable that from Fig. 3.3 (c), r_B values of L_113 seemed to reach its peak around the current level 3×10^{-3} A/μm^2. Finally, as the current levels were increased up to 10^{-2} A/cm^2, $J_M(y)$ and $J_L(y)$ became much similar each other. It was consistent with the measurement results in Fig. 3.3 (c) that the r_B values of the devices M_113 and L_113 were in similar levels and decayed with increasing the bias current as the bias current was larger than 10^{-2} A/cm^2.

According to the simulational results above, the physical behaviors of r_E and r_B were identified. The values of r_E were nearly invariant to the bias current density. In contrast, the vertical current spreading effect which induced r_B rising with current density level would behave more apparently for modern bipolar devices resulting from their reducing effective intrinsic base thickness and emitter width for high f_T. Such phenomena could impact the RF characteristics discussed below.

3.4 Impacts on Cutoff Frequency and maximum Oscillation Frequency

Figures 3.5 (a), (b) and (c) illustrated the f_T-J_C and f_{max}-J_C of devices with different geometries and doping profiles. In Fig. 3.5 (a), all of the devices had the fixed emitter widths and lengths yet in different emitter strip number N_E. It was observed that the current density levels J_{TP} and J_{mP} on which the peak f_T and f_{max} took place were inconsistent. As illustrated in Fig. 3.5 (a), the deviation between J_{TP} and J_{mP} would grow larger as the emitter length L_E or number of emitter strip N_E decreased. Moreover, as the emitter width increased, such deviation illustrated in Fig. 3.5 (b) shrank. In addition, for devices in the fixed geometry, devices in group H resulted in most significant divergence between J_{TP} and J_{mP} compared with that of devices in group M and L, as observed in Fig. 3.5 (c). Such phenomena discussed above impacted the RF characteristics of the transistor since the optimum bias condition for power gain consideration did not agree with the bias condition low-noise and low-intermodulation requirements [10, 11]. In order to further analyze the cause of such phenomena, theoretic derivations for obtaining f_T and f_{max} based on the small signal model illustrated in Figure 3.2 (c) were illustrated in the following paragraph.

3.5 Mathematical Verifications

Fig. 3.2 (c) illustrated the high-frequency small signal model of a SiGe HBT with the source and load impedance of testing equipment, R_S and R_L respectively. The formulas were derived based on the definitions of f_T and f_{max} associated with fundamental network theorem:

$$i_B = i_\mu + i_\pi \tag{1.1}$$

$$i_C = g_m v_\pi - i_\mu \tag{1.2}$$

$$v_B = i_b r_E + i_\pi Z_\pi + (1 + g_m Z_\pi) i_\pi r_E \tag{1.3}$$

$$v_B = i_b r_E + i_\mu Z_\mu - i_C (r_C + Z_L) \tag{1.4}$$

Based on the Eq. 1.1 to Eq. 1.4, the current gain with Z_L could be obtained:

$$\begin{aligned} h_{fe}(jw) &= \frac{ic}{ib} = \frac{\dfrac{1}{1 + jwC_{CS}(Z_L + r_C)}\left\{g_m Z_\pi - \left[\dfrac{Z_\pi}{Z_\mu} + (1 + g_m Z_\pi)\dfrac{r_E}{Z_\mu}\right]\right\}}{1 + \dfrac{Z_\pi}{Z_\mu} + (1 + g_m Z_\pi)\dfrac{Z_o' + r_E}{Z_\mu}} \\ &= \frac{\left\{\left[g_m - jwC_\mu(1 + g_m r_E)\right]\left(\dfrac{r_\pi}{1 + jwC_\pi r_\pi}\right) - jwC_\mu r_E\right\}\dfrac{1}{1 + jw(Z_L + r_C)C_{CS}}}{1 + jwC_\mu\left(\dfrac{r_C + Z_L}{1 + jw(r_C + Z_L)C_{CS}} + \dfrac{r_\pi}{1 + jwr_\pi C_\pi}\right) + jwC_\mu\left[1 + g_m r_E + \dfrac{g_m(r_C + Z_L)}{1 + jw(r_C + Z_L)C_{CS}}\right]\dfrac{r_\pi}{1 + jwr_\pi C_\pi}} \end{aligned} \tag{2.1}$$

After the first-order approximation, Eq. 2.1 becomes:

$$h_{fe}(jw) \approx \frac{g_m}{jw\left[C_\pi + C_\mu + g_m(r_C + r_E)C_\mu + g_m(r_C + Z_L) + \frac{1}{\beta}C_{CS}(r_C + Z_L)\right]}$$

$$\approx \frac{g_m}{jw\left[C_\pi + C_\mu + g_m(r_C + r_E)C_\mu + g_m(r_C + Z_L)\right]} \tag{2.2}$$

Let w_T' be the cutoff frequency with the load resistance Z_L while w_T was defined as the output short-circuit (Z_L was set to zero) cutoff frequency:

$$h_{fe}(jw) = \frac{w_T'}{jw} \text{ and } \frac{1}{w_T'} = \frac{1}{w_T} + C_\mu Z_L \tag{2.3}$$

$$\frac{1}{w_T} = \frac{1}{g_m}(C_\pi + C_\mu) + (r_C + r_E)C_\mu = \frac{C_{DE}}{g_m} + \frac{C_{BE} + C_{BC}}{g_m} + (r_C + r_E)C_\mu = t_F + t_{JC} + t_{RC} \tag{2.4}$$

From the above formulas, t_F, t_{JC} and t_{RC} were denoted as the forward transit time, junction delay time and RC delay time of the devices. These results agreed with the descriptions in [12]. The power gain was defined as the ratio of the received power on Z_L over the power delivered into the device.

$$G_p(jw) = \frac{P_L}{P_{in}} = \frac{i_c^2 Z_L}{i_b^2 Z_{in}} = h_{fe}^2 \frac{Z_L}{Z_{in}} \tag{3.1}$$

Where Z_{in} denoted the input impedance of the device and the values of r_B were extracted from it at 50 GHz. It could be obtained as the follow:

$$Z_{in} \equiv r_{BE} \approx r_B + (1 + h_{fe})r_E \tag{3.2}$$

Substituting Eq. 3.2 into Eq. 3.1:

$$\left|G_p(jw)\right| = \frac{\left|Z_L\right| w'^2_T}{(r_B + r_E)w^2 + w'_T\, w r_E} \tag{3.3}$$

Let |G (jw)| = 1, the $w_{\max}$ could be obtained as follow:

$$f_{\max} = \frac{w_T'}{2\pi}\left[\sqrt{\frac{r_E^2}{4(r_B + r_E)^2} + \frac{\left|Z_{L\_OPT}\right|}{r_B + r_E}} - \frac{r_E}{2(r_B + r_E)}\right] \tag{3.4}$$

Eq. 3.4 reflected the effects of the emitter resistance that did not considered in [11]. As R_{L_OPT} was the complex conjugate of the output impedance of the transistor z_{out}, which made the transistor have the maximum power gain as illustrated as follow:

$$\left|Z^*_{L\_OPT}\right| = \left|z_{out}\right| = \left| r_C + \frac{1}{jwC_{BC}} \frac{\left(\frac{1}{r_B} + \frac{1}{Z_\pi} + jwC_{BC}\right)\left(r_E + \frac{Z_\pi}{1 + g_m Z_\pi}\right) - \frac{r_E}{Z_\pi}}{1 + \frac{1}{r_B}\left(\frac{Z_\pi}{1 + g_m Z_\pi}\right)} \right| \quad \text{and}$$

$$Z_\pi = \frac{1}{jwC_\pi} // r_\pi \tag{3.5}$$

Based on Eqs. 3.2 to 3.5, the rationality that r_B rising induced the splitting between J_{TP} and J_{mP} could be identified. In addition, the value of J_{mP} would be lower than that of J_{TP} if r_B value was rapidly increased around the bias current level J_{TP}. This deduction was identified in the previous measurement results illustrated in Figs. 3.3 (a), (b) and (c) along with Figs. 3.5 (a), (b) and (c). They had shown the entire agreement with the qualitative deduction that group H devices would result in the largest divergence between J_{TP} and J_{mP} resulting from its rapid increase of r_B value around its J_{TP}. On the contrary, for group L devices, J_{TP} appeared on the value around which r_B rising slop was much lower than that of H-group devices and the peak values of r_B for group L devices were also much lower than that of H-group devices. It resulted in little inconsistency between J_{TP} and J_{mP} for L-group devices. The following numerical verification would be further used to identify the deduction validity in a quantitative way.

Figures 3.6 (a), (b) and (c) illustrated the relationships between measured (f_{max_meas}) and estimated (f_{max_cal}) maximum oscillation frequencies of devices H_113, M_115 and L_111 along with their corresponding measured f_T (f_{T_meas}) and extracted r_B. The parameters involved in f_{max} estimation including the emitter resistance r_E, collector resistances r_C and base to collector capacitance C_{BC} (or C_μ) were listed in Tables 3.3 (a), (b) and (c), respectively. Although there were larger estimation deviations between f_{max_cal} and f_{max_meas} on high current levels far away from the interested bias conditions in this study, the estimated values f_{max_cal} agreed with the measured values f_{max_meas} well and it could verify the quantitative deduction in different ways.

3.6 Conclusion

In this article, the current dependency of r_B was reported and analyzed. It was discovered that the value of r_B would be increased with increasing current density especially for devices with narrow intrinsic base thickness and small emitter widths. The associated physical model was created based on the measurement relationships of

r_B-J_B and identified by MEDICI simulation. Such phenomena also impacted the RF characteristics of SiGe HBT devices by splitting the current levels J_{TP} and J_{mP} on which f_T and f_{max} could reach their peak values. Theoretic derivation and numerical verification had been performed to identify the deduction that the behavior of r_B should take this responsibility. Unfortunately, for applications with low power consumption, small-sized devices would be widely applied and such phenomena could be fairly harmful to RF performances. Therefore, for fixed device area which could afford sufficient driving power, enlarging the emitter width would be suggested for suppressing the r_B rising effect and improving the RF performance of the device. However, it may sacrifice f_{max} of the device.

References

[1] Ingvarson, F., Linder, M., Jeppson, K.O., "Extraction of the base and emitter resistances in bipolar transistors using an accurate base resistance model", in *IEEE Trans.*, vol. 16, Issue 2, pp. 228 -232, 2003

[2] Zimmer, T., Berkner, J., Branciard, B., "Method for determining the effective base resistance of bipolar transistors", *IEEE BCTM*, pp. 122 - 125, 1996

[3] King, C.A., Johnson, R.W., Chen, Y.K., "Integratable and low base resistance

Si/Si1-xGex heterojunction bipolar transistors using selective and non-selective rapid thermal epitaxy", *IEEE IEDM*, pp. 751 - 754, 1995

[4] Verzellesi, G., Vendrame, L., Turetta, R.,"A new experimental technique for extracting base resistance and characterizing current crowding phenomena in bipolar transistors", *IEEE IEDM*, pp. 413 -416, 1992

[5] David J. Roulston, "Voltage- and Current- Dependent Model of the Base Resistance of Bipolar Transistor", *IEEE Trans. Vol. 35*, 1988

[6] Agilent ICCAP Manue, "High Frequency Modeling Technology"

[7] David J. Roulston, "Voltage- and Current- Dependent Model of the Base Resistance of Bipolar Transistor", *IEEE Trans. Vol. 35*, 1988

[8] Guofu Niu, "The effects of Gepmetrical Scaling on the Frequency Response and Noise Performance of SiGe HBT.", *IEEE Trans. vol. 49,* 2002.

[9] Mani Vaidyanathan "A Theory of High-Frequency Distortion in Bipolar Transistors", *IEEE Trans.*, 2003

[10] Yuan Taur, "Fundamentals of Modern VLSI Devices", p. 382, 1998

Figures and Tables in Chapter 3

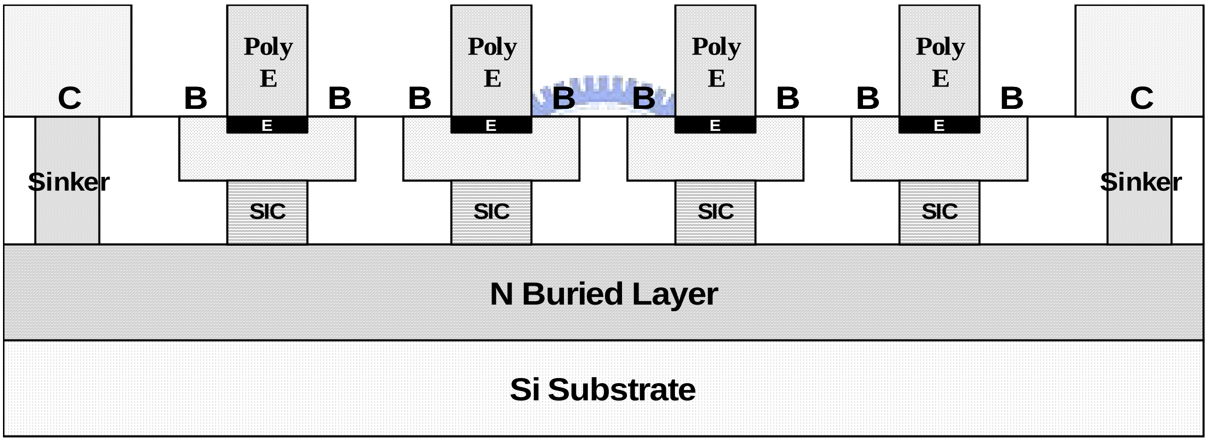

Cross-section of view of SiGe HBT devices if 4 emitter strips

Figure 3.1 (a)

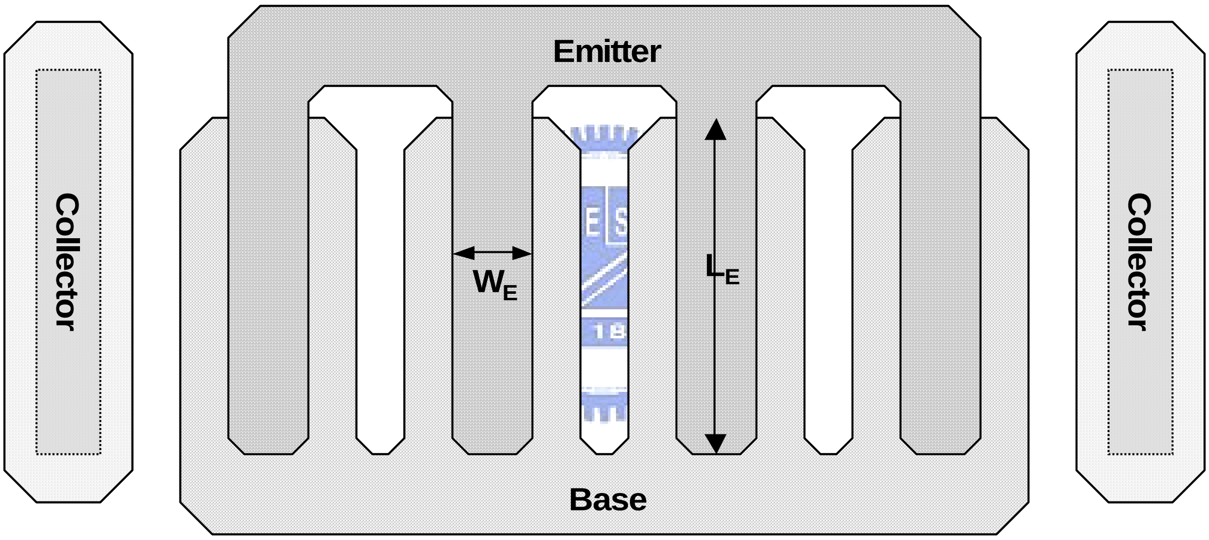

Top view of SiGe HBT devices if 4 emitter strips

Figure 3.1 (b)

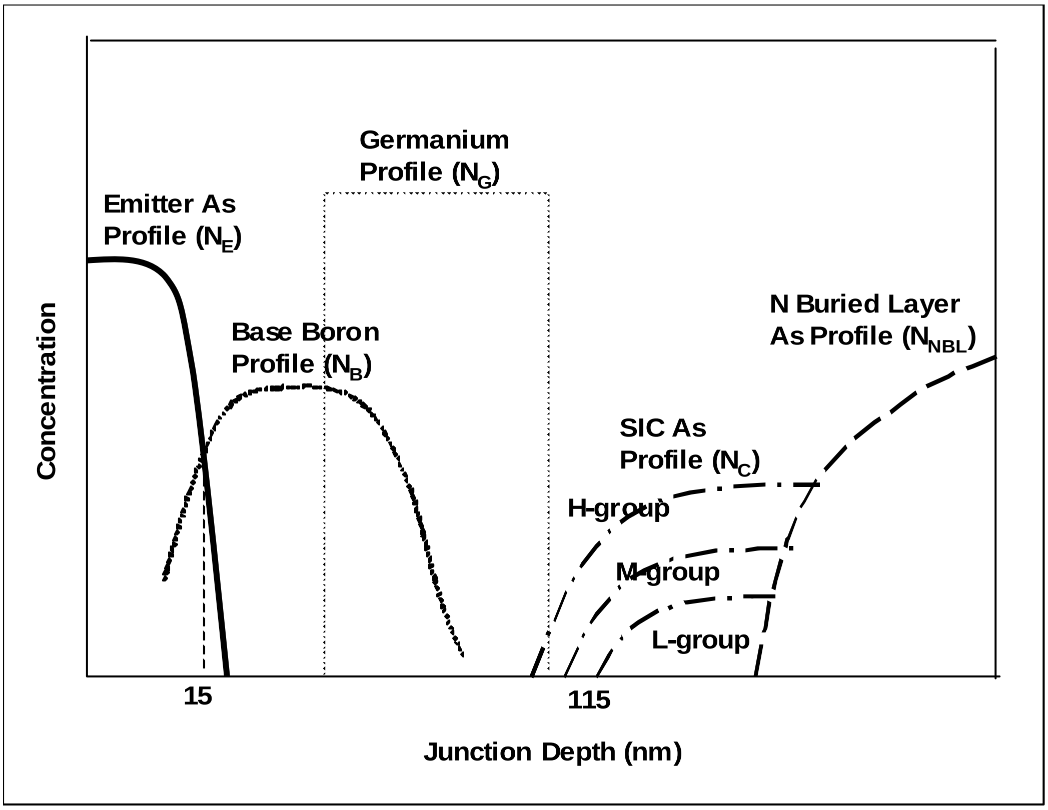

Doping profile of 0.18 μm SiGe HBT devices with heavily (H-group), medium (M-group) and lightly (L-group) SIC doping levels.

Figure 3.1 (c)

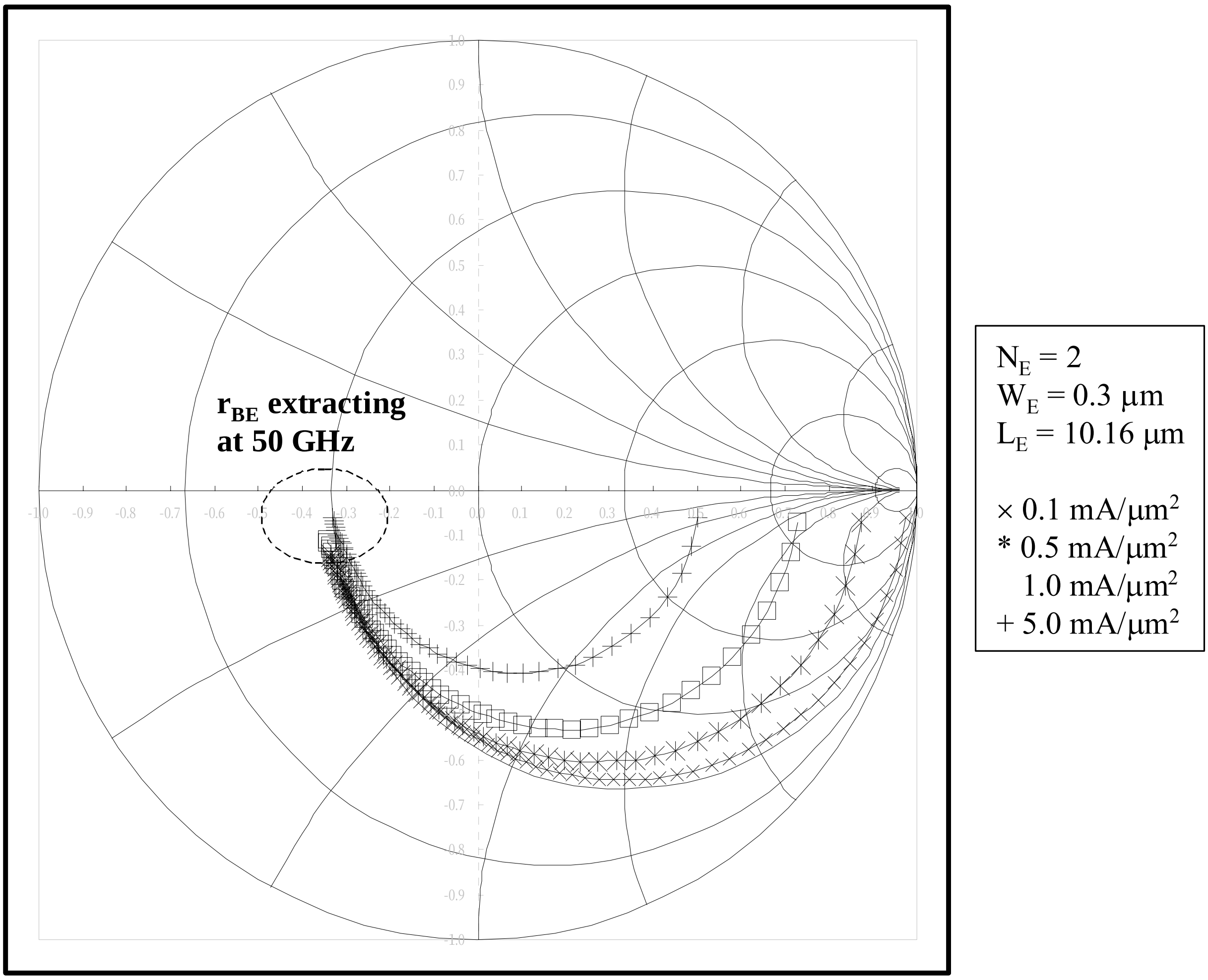

Input scattering coefficient S_{11} of SiGe HBT under various bias conditions and corresponding r_{BE} extraction locations in Smith plane

Figure 3.2 (a)

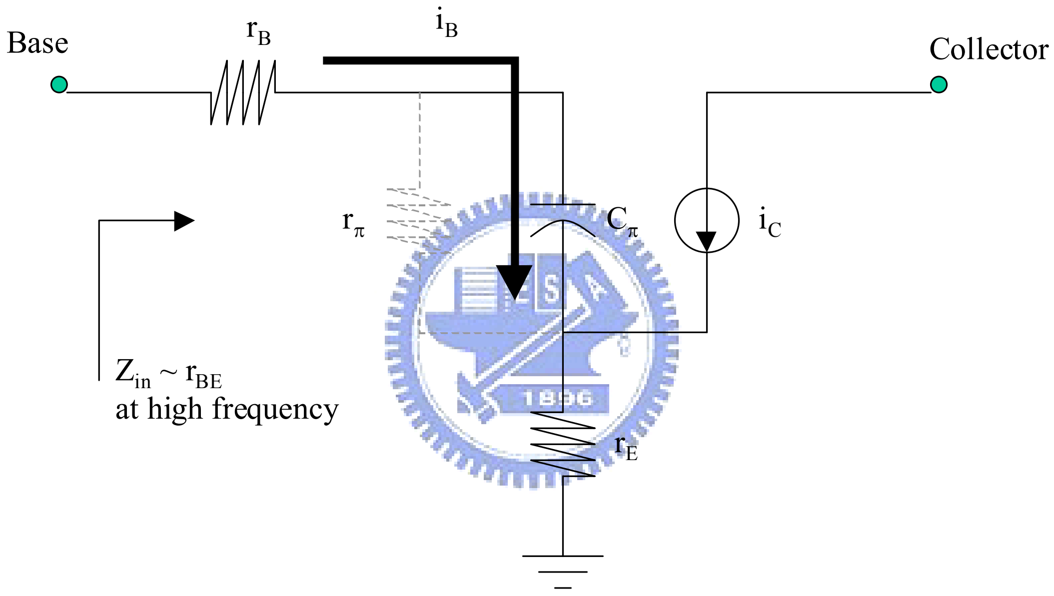

Schematic illustration of r_B extraction methodology

Figure 3.2 (b)

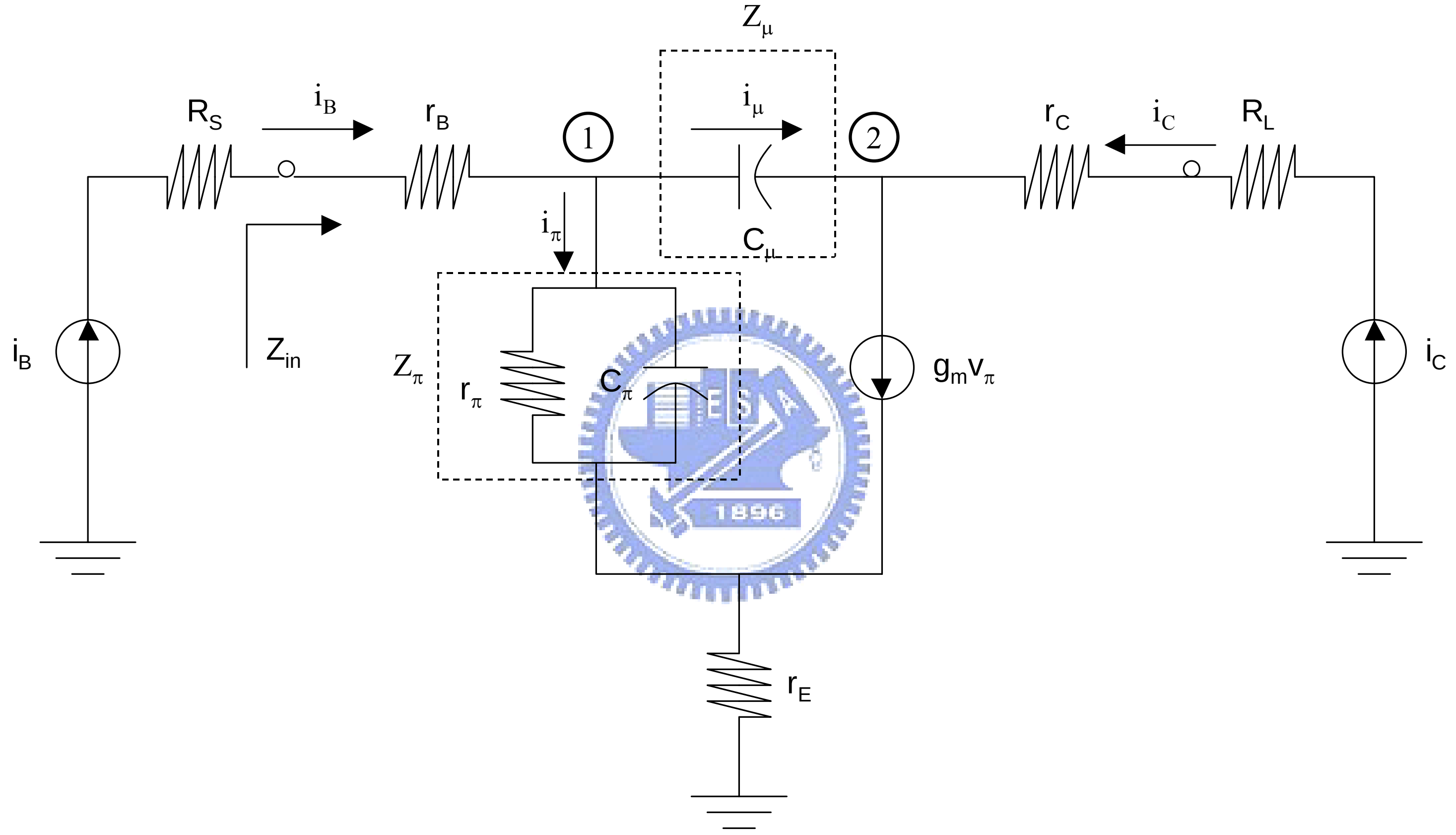

RF small signal model of bipolar device with emitter resistance

Figure 3.2 (c)

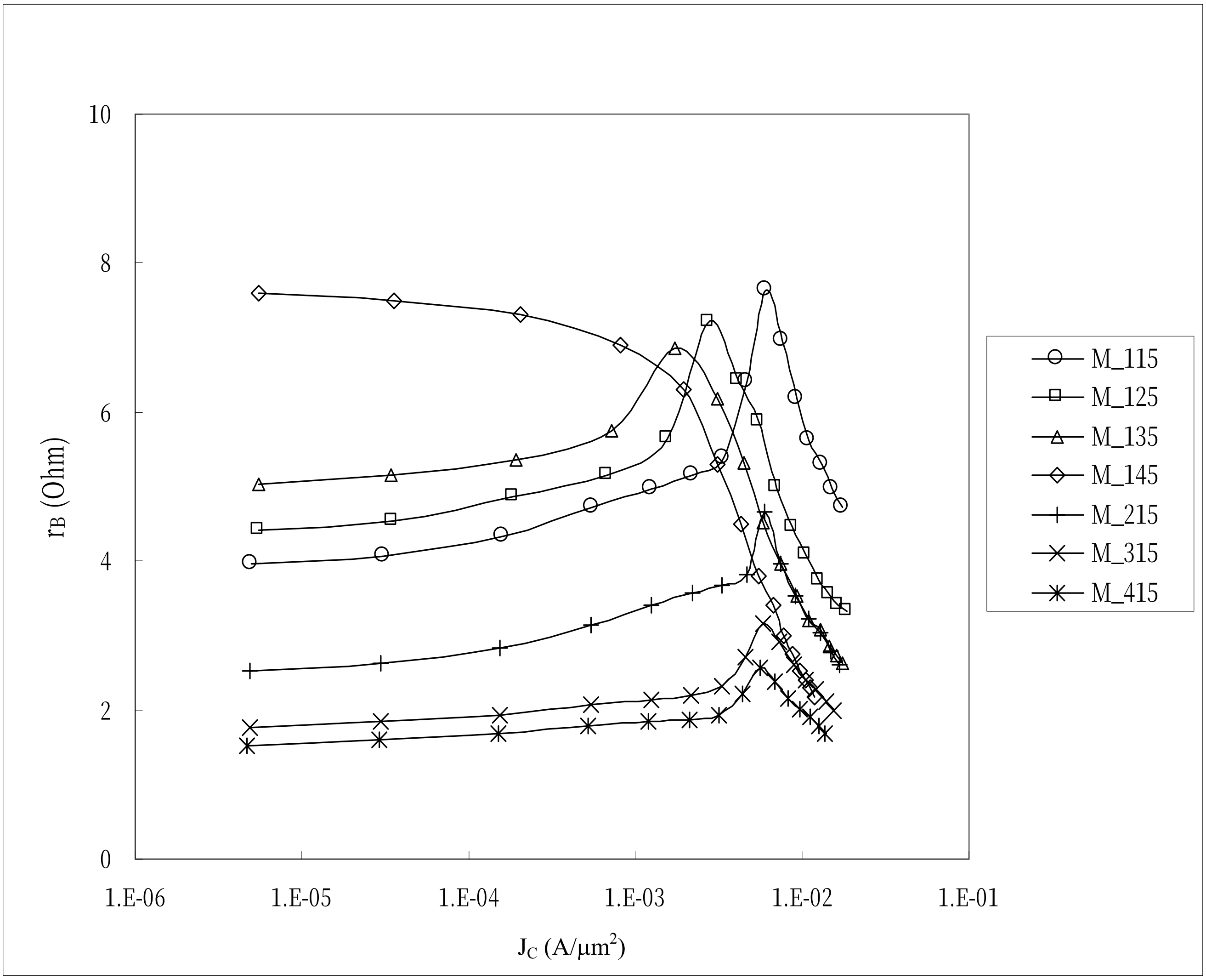

Measurement result of r_B-J_C relationships of HBT devices in various geometry

Figure 3.3 (a)

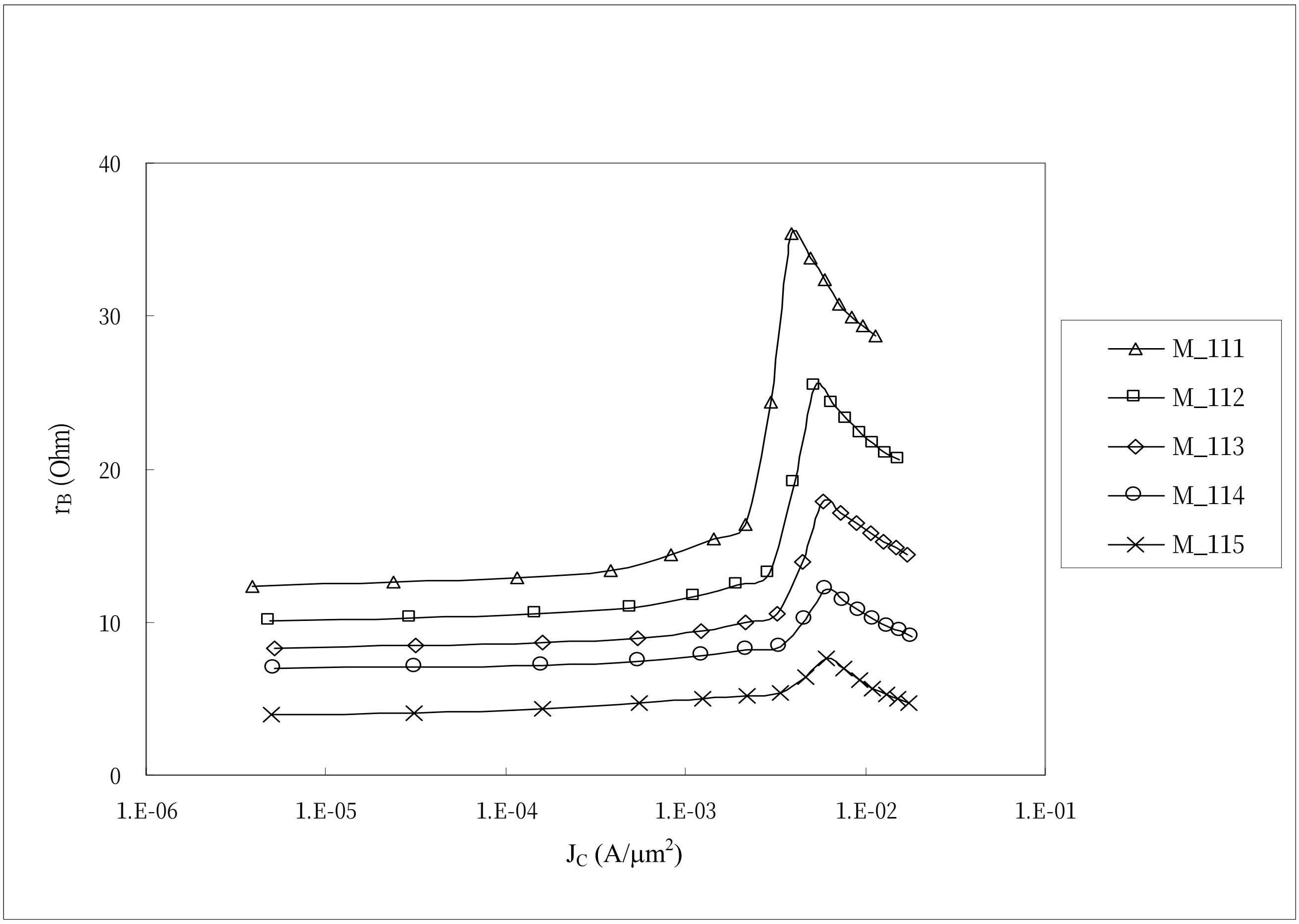

Measurement result of r_B-J_C relationships of HBT devices in various emitter length

Figure 3.3 (b)

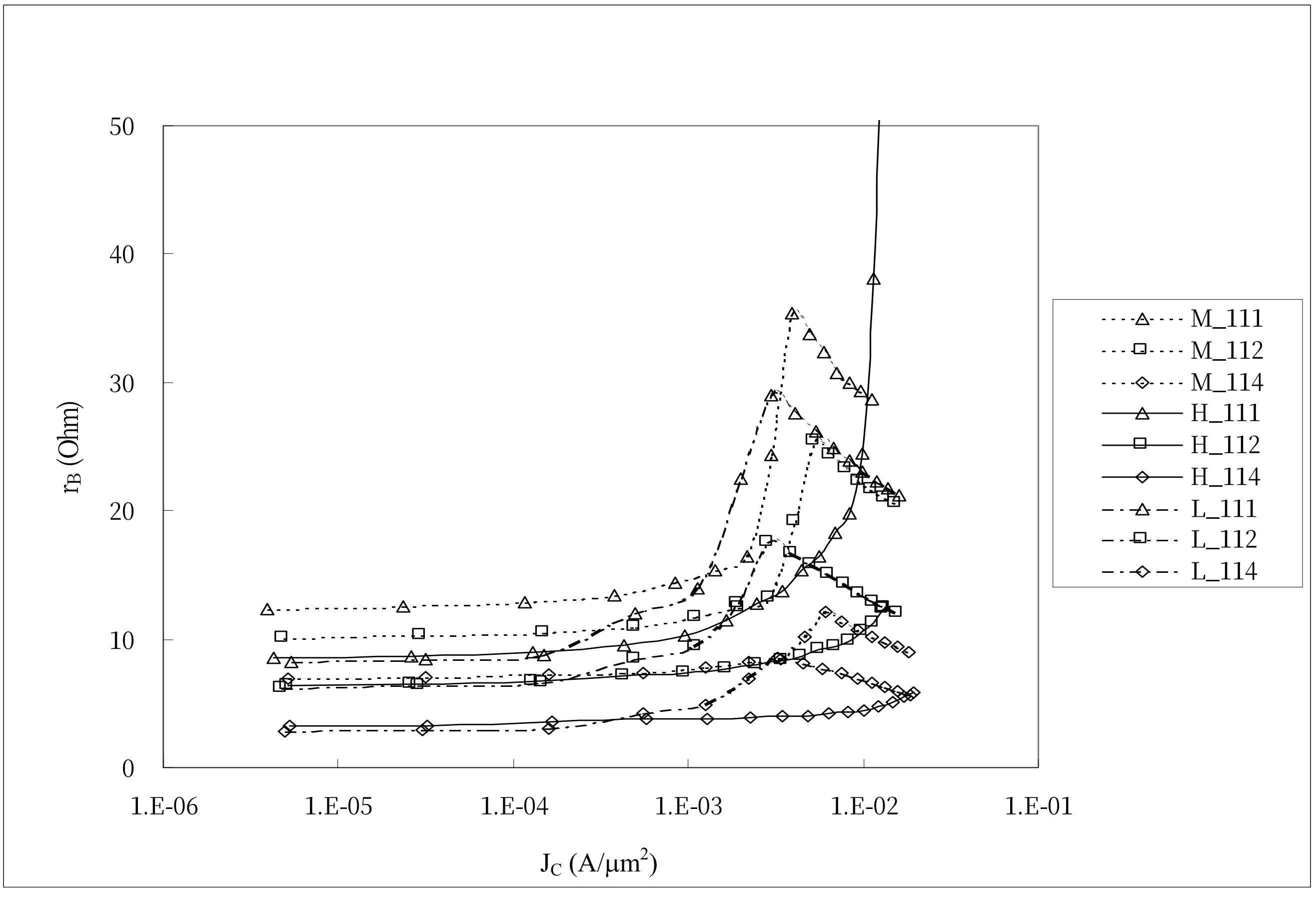

Measurement result of r_B-J_C relationships of HBT devices in various SIC doping levels

Figure 3.3 (c)

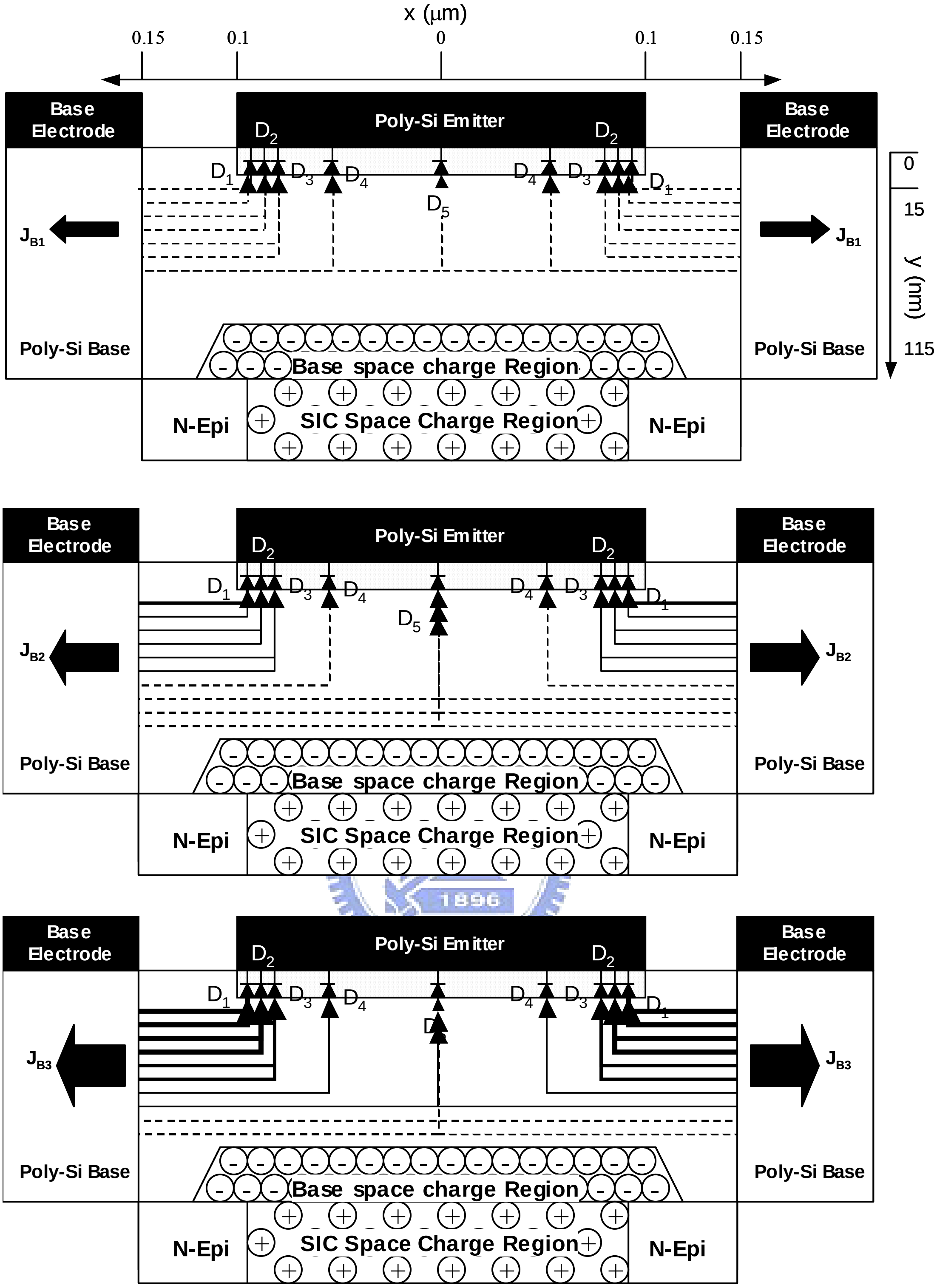

Current flux modulation in the pinch base region of L-group SiGe HBT devices under low (J_{B1}), medium (J_{B2}) and high (J_{B3}) current levels

Figure 3.4 (a)

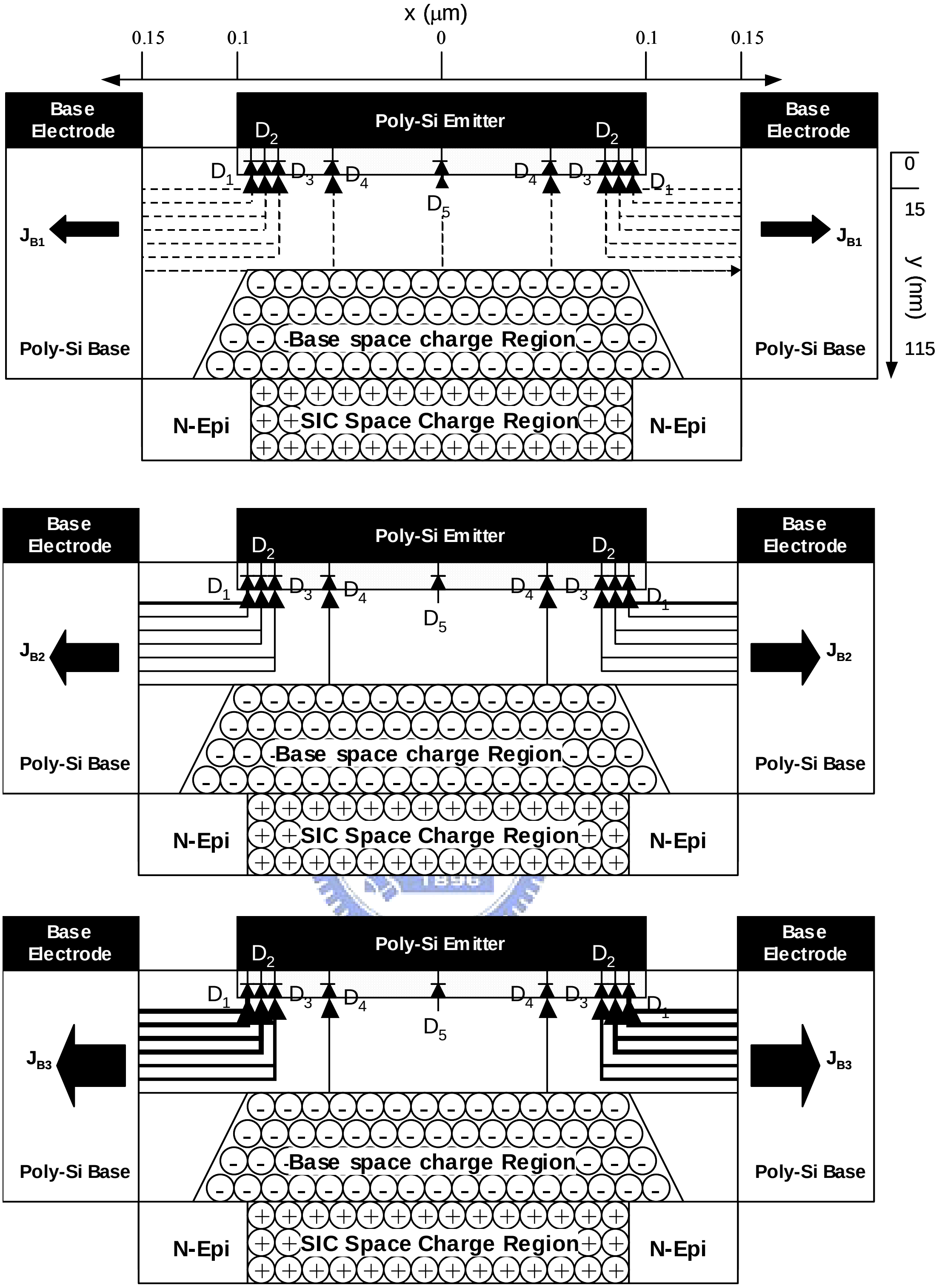

Current flux modulation in the pinch base region of M-group SiGe HBT devices under low (J_{B1}), medium (J_{B2}) and high (J_{B3}) current levels

Figure 3.4 (b)

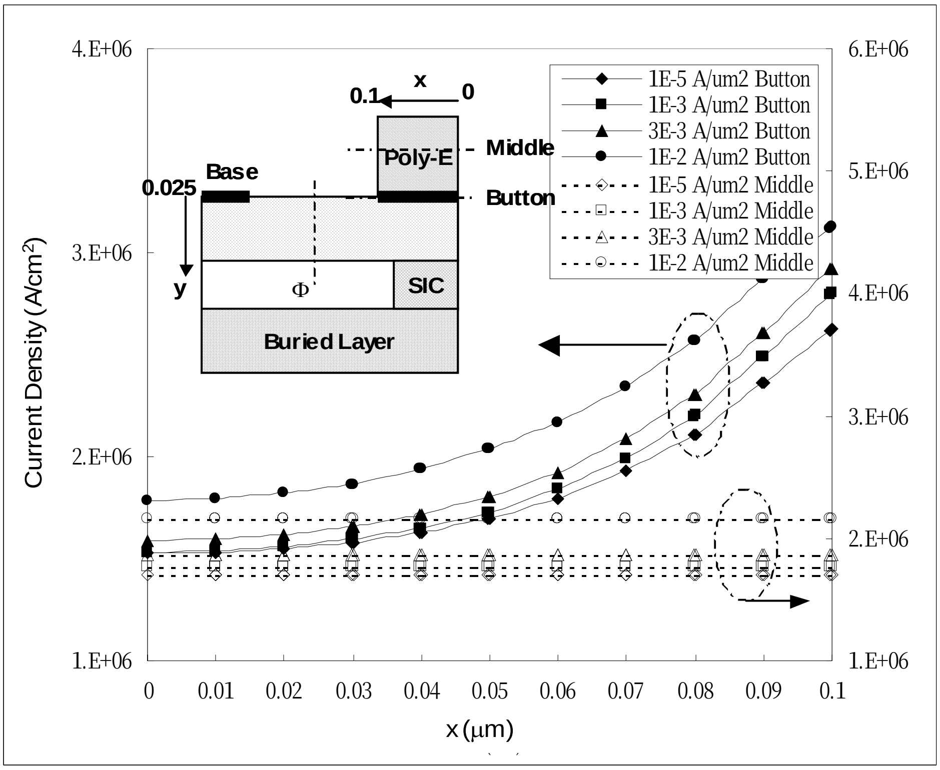

MEDICI simulation results on the Middle and Button planes in the poly silicon emitter under various bias conditions

Figure 3.4 (c)

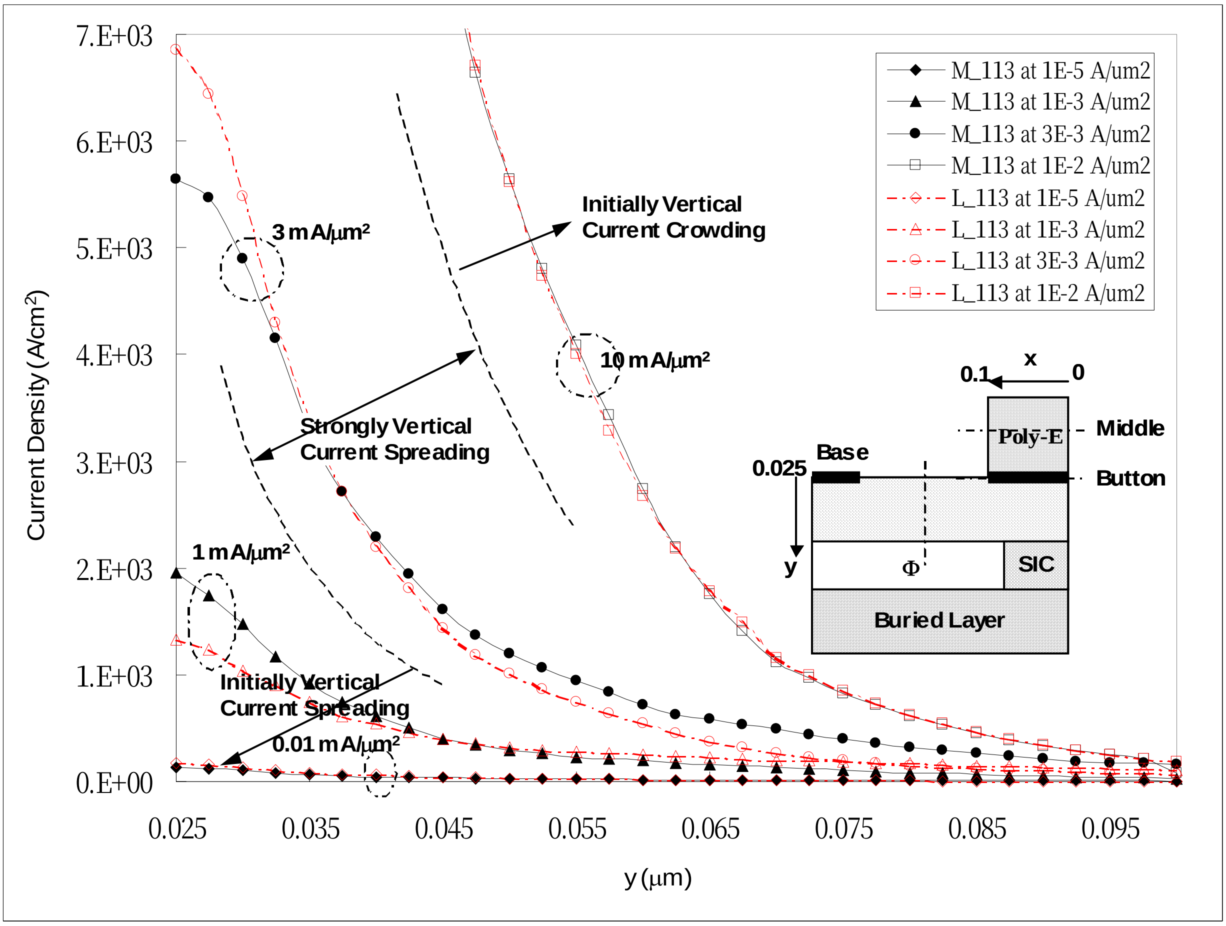

MEDICI simulation results on plane Φ in the pinch base region under various bias conditions

Figure 3.4 (d)

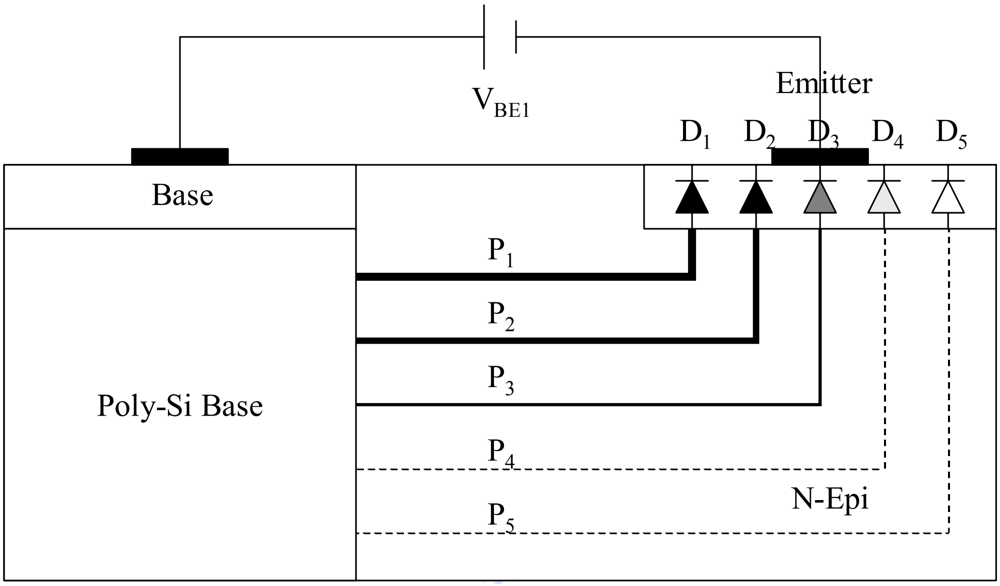

Current flux and corresponding PN junction of base-emitter region under low current level

Figure 3.4 (e)

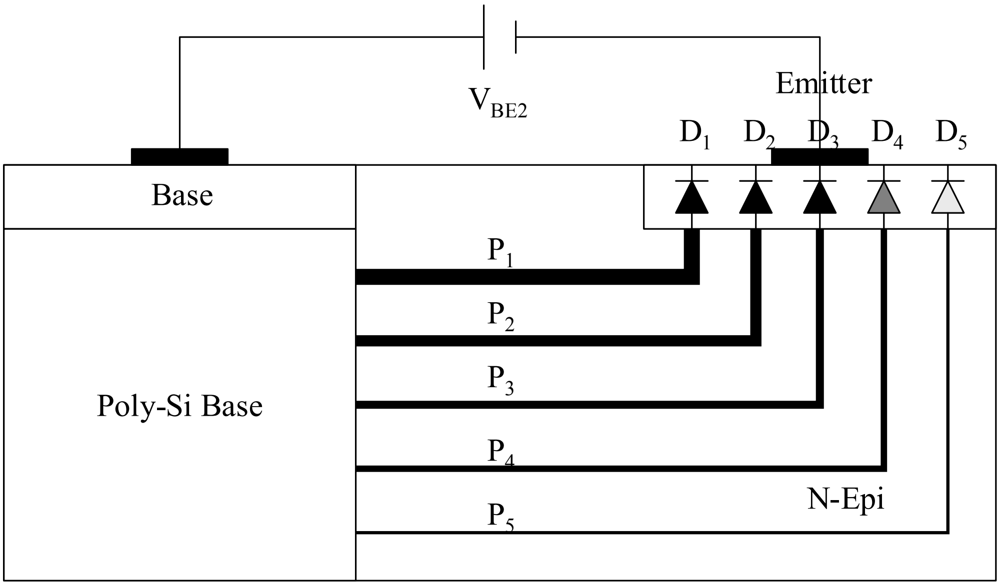

Current flux and corresponding PN junction of base-emitter region under high current level

Figure 3.4 (f)

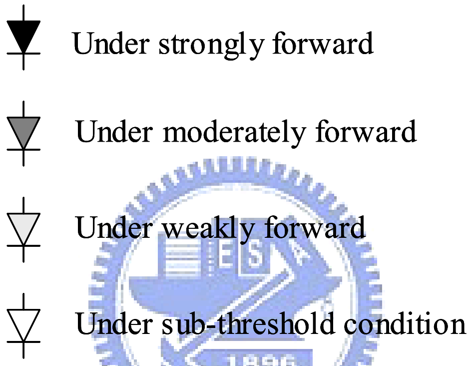

Symbol illustration of the PN junction diodes under various bias conditions

Figure 3.4 (g)

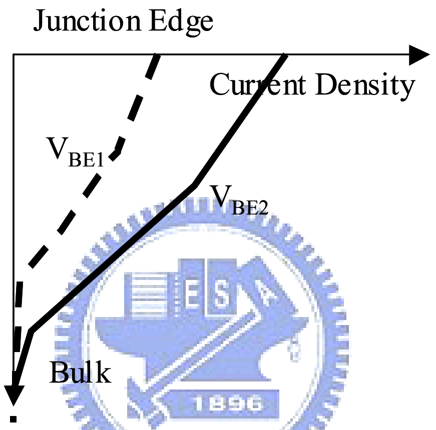

Schematic current density distribution in the pinch base region under V_{BE1} and V_{BE2} bias conditions

Figure 3.4 (h)

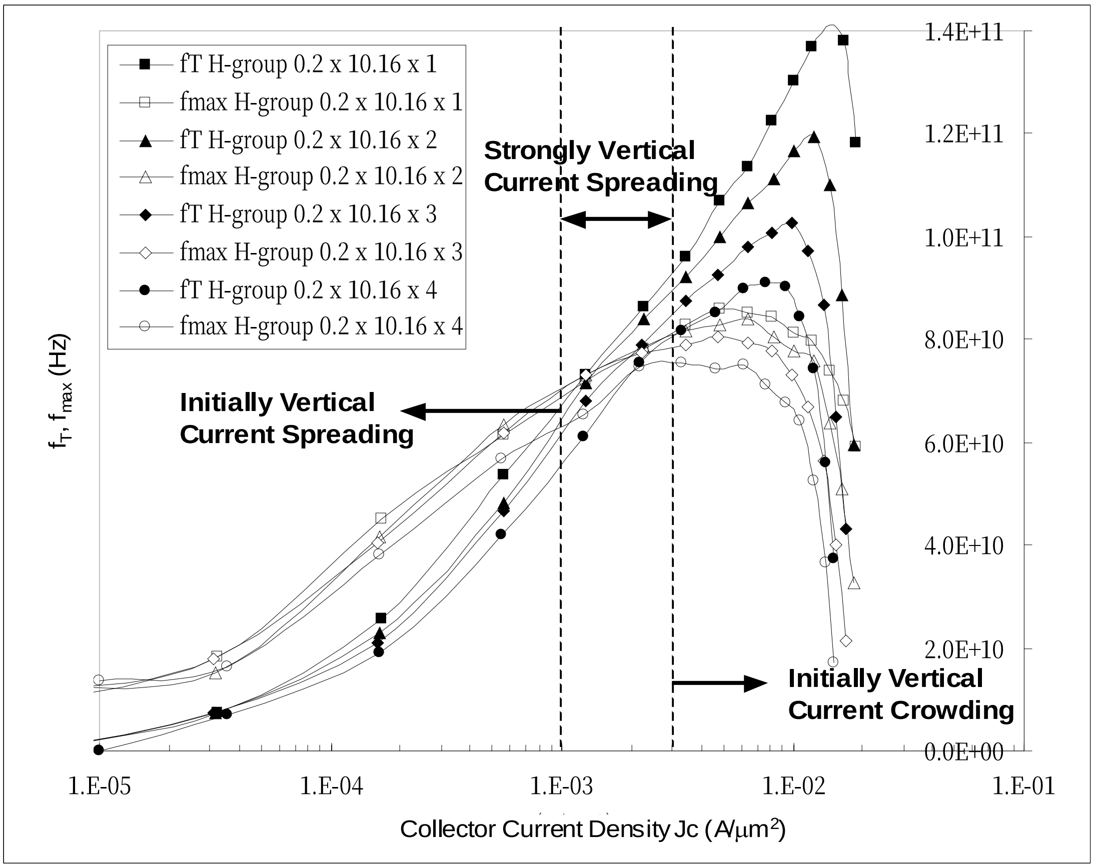

f_T, f_{max} versus J_C of HBT devices in various emitter strip numbers

Figure 3.5 (a)

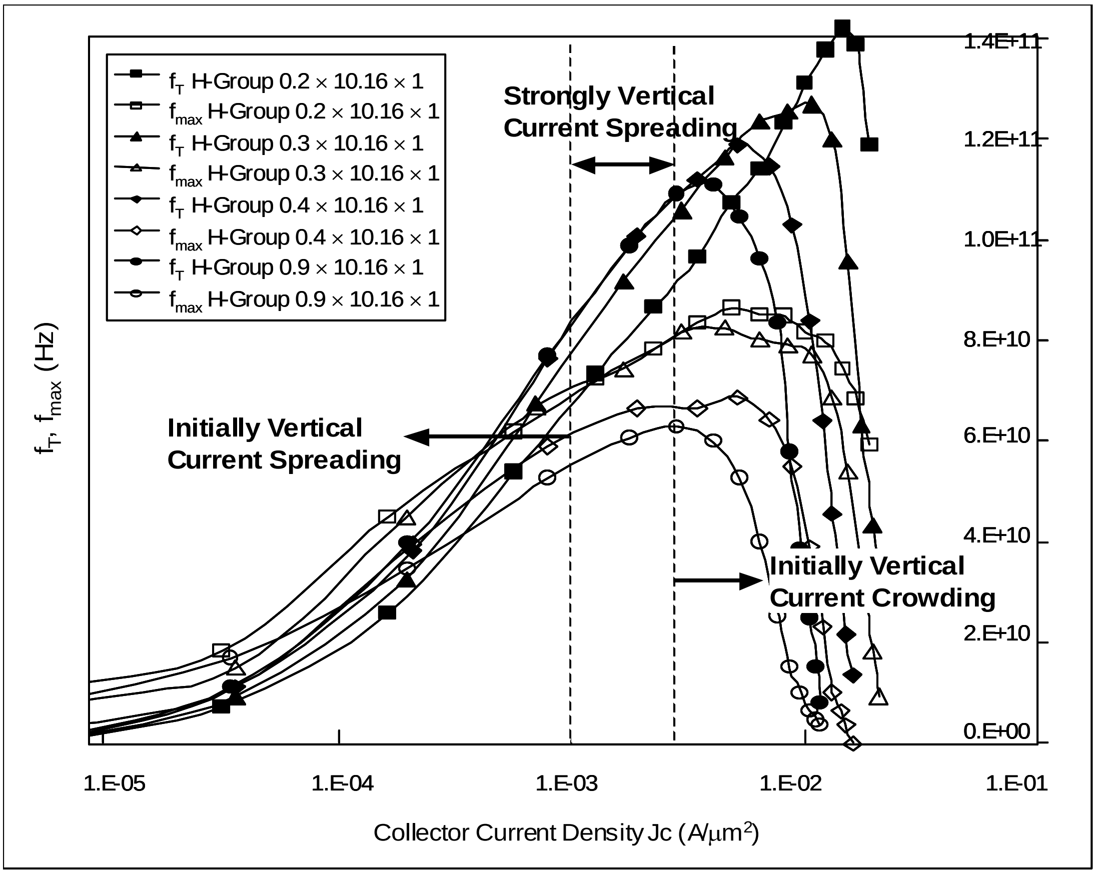

f_T, f_{max} versus J_C of HBT devices in various emitter widths

Figure 3.5 (b)

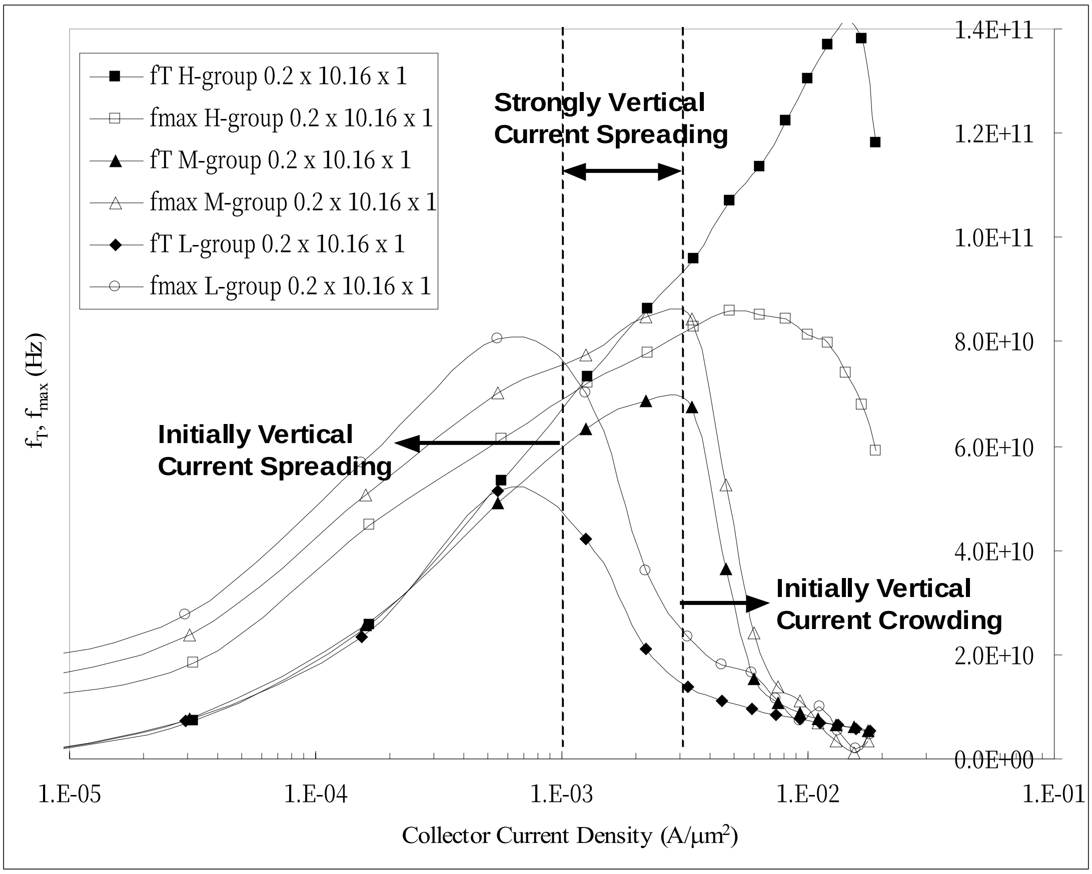

f_T, f_{max} versus J_C of HBT devices in various SIC doping levels

Figure 3.5 (c)

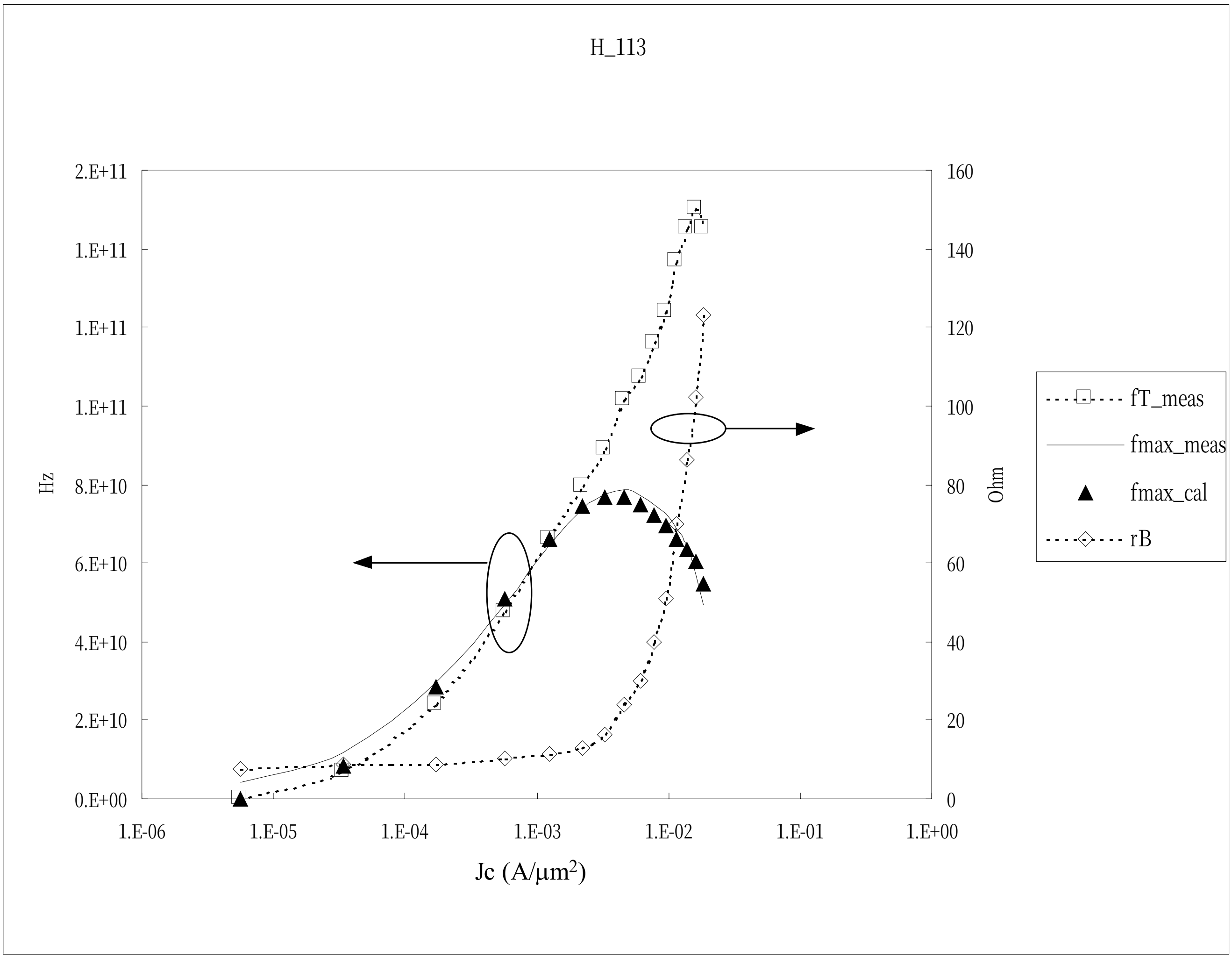

Measure f_T, f_{max} and r_B-J_C and estimated f_{max}-J_C relationships of H-group HBT devices

Figure 3.6 (a)

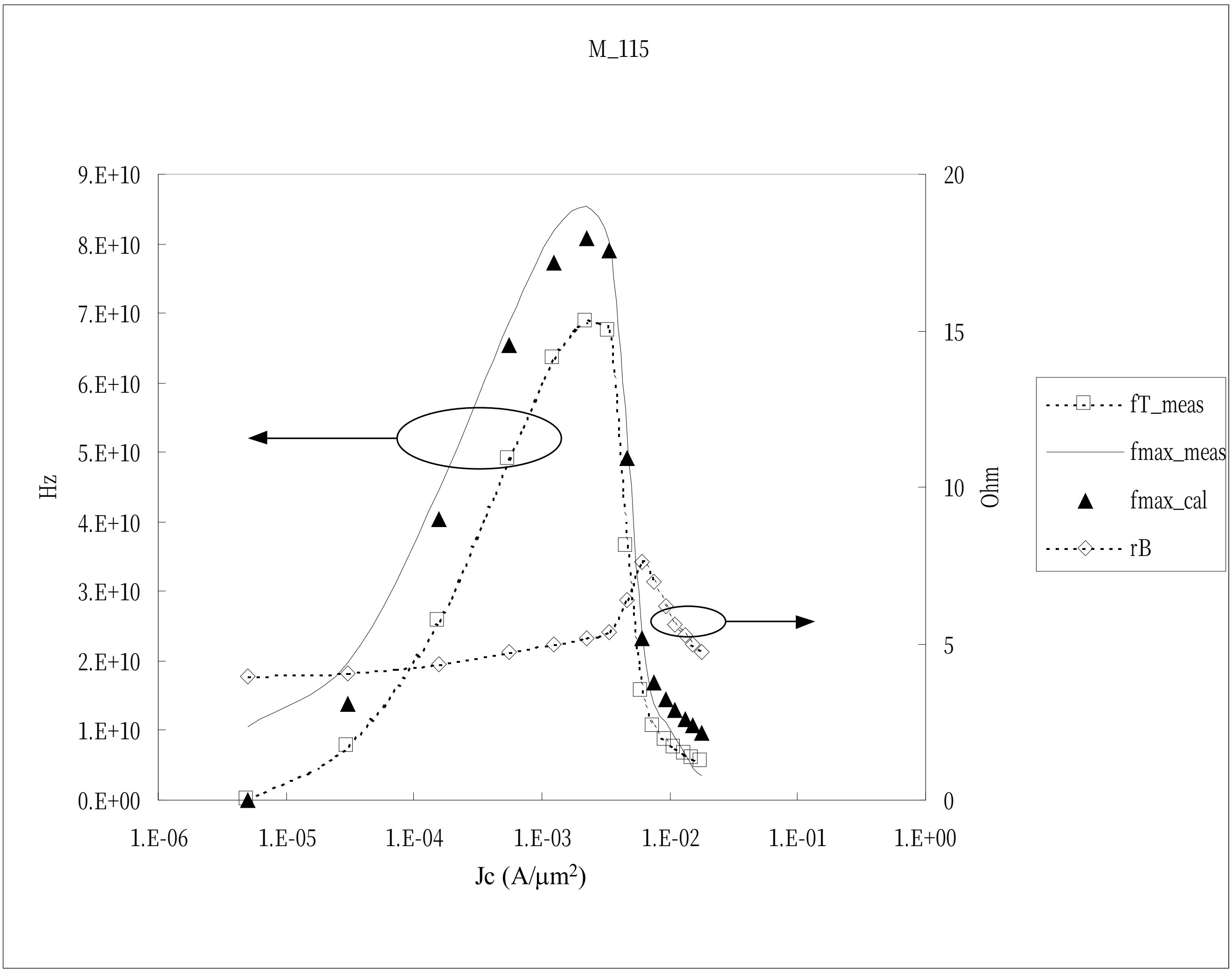

Measure f_T, f_{max} and r_B-J_C and estimated f_{max}-J_C relationships of M-group HBT devices

Figure 3.6 (b)

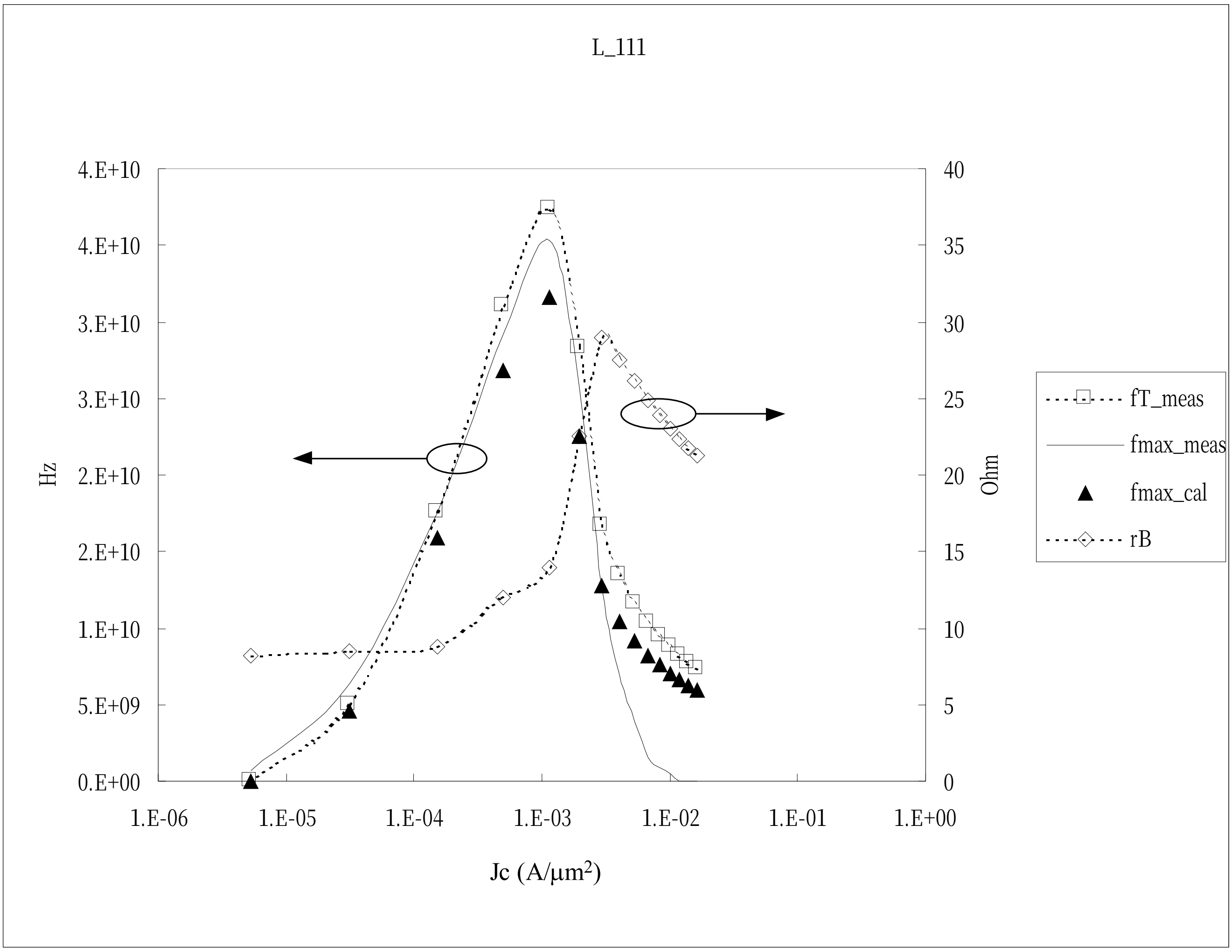

Measure f_T, f_{max} and r_B-J_C and estimated f_{max}-J_C relationships of L-group HBT devices

Figure 3.6 (c)

Parameters yz					
$W_{E\,(um)}$ \ $L_{E\,(um)}$	0.76	1.76	2.64	4.52	10.16
0.2	11	12	13	14	15
0.3	21	22	23	24	25
0.4	31	32	33	34	35
0. 9	41	42	43	44	45
Parameter x					
no. of strip	1	2	3	4	
x	1	2	3	4	
Doping Proifle					
Group	H	M	L		
SIC Layer	Heavy	Light	None		

Mapping of between of device naming and corresponding geometry in this research

Table 3.1

Device	M_111	M_112	M_113	M_114	M_115	M_125	M_135	M_155	M_215	M_315	M_415
r_E (Ohm)	8.9	6.68	4.9	3.56	2.56	3.21	3.84	6.4	1.41	0.97	0.73

Measured emitter resistance of HBT devices in various geometry

Table 3.2

Devices Parameters H_113				
Jc (A/um2)	rB (Ohm)	fT_meas	fmax_meas	fmax_cal
5.55E-06	7.41E+00	1.72E+06	4.36E+09	2.28E+06
3.38E-05	8.71E+00	6.68E+09	1.18E+10	8.42E+09
1.70E-04	8.91E+00	2.39E+10	2.97E+10	2.84E+10
5.68E-04	1.02E+01	4.74E+10	4.95E+10	5.11E+10
1.26E-03	1.13E+01	6.60E+10	6.46E+10	6.61E+10
2.19E-03	1.30E+01	7.94E+10	7.38E+10	7.43E+10
3.32E-03	1.65E+01	8.90E+10	7.75E+10	7.69E+10
4.61E-03	2.40E+01	1.01E+11	7.86E+10	7.69E+10
6.09E-03	3.00E+01	1.07E+11	7.73E+10	7.50E+10
7.74E-03	4.01E+01	1.16E+11	7.48E+10	7.21E+10
9.56E-03	5.11E+01	1.24E+11	7.26E+10	6.95E+10
1.16E-02	7.01E+01	1.37E+11	6.88E+10	6.60E+10
1.37E-02	8.61E+01	1.45E+11	6.46E+10	6.34E+10
1.60E-02	1.02E+02	1.50E+11	5.70E+10	6.05E+10
1.83E-02	1.23E+02	1.45E+11	4.93E+10	5.47E+10

List of measured and estimated values of r_B, f_T and f_{max} versus current density J_C in Fig. 3.6 (a)

Table 3.3 (a)

Devices Parameters M_115

Jc (A/um2)	rB (Ohm)	fT_meas	fmax_meas	fmax_cal
5.00E-06	3.96E+00	1.87E+07	1.06E+10	3.63E+07
3.07E-05	4.07E+00	7.59E+09	1.97E+10	1.38E+10
1.59E-04	4.34E+00	2.57E+10	4.45E+10	4.05E+10
5.49E-04	4.73E+00	4.90E+10	6.87E+10	6.54E+10
1.26E-03	4.96E+00	6.34E+10	8.18E+10	7.73E+10
2.21E-03	5.16E+00	6.87E+10	8.53E+10	8.08E+10
3.36E-03	5.39E+00	6.74E+10	8.04E+10	7.90E+10
4.68E-03	6.41E+00	3.64E+10	5.26E+10	4.93E+10
6.06E-03	7.63E+00	1.55E+10	2.41E+10	2.33E+10
7.54E-03	6.96E+00	1.06E+10	1.38E+10	1.68E+10
9.20E-03	6.18E+00	8.66E+09	1.11E+10	1.44E+10
1.10E-02	5.63E+00	7.52E+09	8.97E+09	1.29E+10
1.31E-02	5.29E+00	6.69E+09	6.59E+09	1.17E+10
1.53E-02	4.96E+00	6.02E+09	4.56E+09	1.07E+10
1.76E-02	4.72E+00	5.42E+09	3.54E+09	9.77E+09

List of measured and estimated values of r_B, f_T and f_{max} versus current density J_C in Fig. 3.6 (b)

Table 3.3 (b)

Devices Parameters L_111				
Jc (A/um2)	rB (Ohm)	fT_meas	fmax_meas	fmax_cal
5.33E-06	8.19E+00	4.23E+04	6.45E+08	3.91E+04
3.12E-05	8.46E+00	4.99E+09	6.38E+09	4.58E+09
1.51E-04	8.74E+00	1.76E+10	1.75E+10	1.59E+10
5.01E-04	1.20E+01	3.10E+10	2.92E+10	2.69E+10
1.13E-03	1.40E+01	3.73E+10	3.54E+10	3.16E+10
1.97E-03	2.25E+01	2.83E+10	2.58E+10	2.25E+10
2.96E-03	2.90E+01	1.67E+10	1.27E+10	1.27E+10
4.08E-03	2.76E+01	1.35E+10	6.88E+09	1.04E+10
5.33E-03	2.62E+01	1.17E+10	3.90E+09	9.13E+09
6.72E-03	2.49E+01	1.04E+10	1.60E+09	8.23E+09
8.26E-03	2.39E+01	9.47E+09	8.41E+08	7.56E+09
9.96E-03	2.30E+01	8.77E+09	4.61E+08	7.06E+09
1.18E-02	2.23E+01	8.21E+09	0.00E+00	6.65E+09
1.39E-02	2.18E+01	7.72E+09	0.00E+00	6.28E+09
1.62E-02	2.12E+01	7.31E+09	0.00E+00	5.97E+09

List of measured and estimated values of r_B, f_T and f_{max} versus current density J_C in Fig. 3.6 (c)

Table 3.3 (c)